

Ionization and dissociation induced fragmentation of a tidally disrupted star into planets around a supermassive black hole

KIMITAKE HAYASAKI,¹ MATTHEW R. BATE,² AND ABRAHAM LOEB³

¹*Department of Astronomy and Space Science, Chungbuk National University, Cheongju 361-763, Republic of Korea*

²*School of Physics, University of Exeter, Stocker Road, Exeter EX4 4QL*

³*Harvard-Smithsonian Center for Astrophysics, 60 Garden Street, Cambridge, MA 02138, USA*

(Received June 1, 2019; Revised January 10, 2019; Accepted January 14, 2020)

Submitted to AJ

ABSTRACT

We show results from the radiation hydrodynamics (RHD) simulations of tidal disruption of a star on a parabolic orbit by a supermassive black hole (SMBH) based on a three-dimensional smoothed particle hydrodynamics code with radiative transfer. We find that such a tidally disrupted star fragment and form clumps soon after its tidal disruption. The fragmentation results from the endothermic processes of ionization and dissociation that reduce the gas pressure, leading to local gravitational collapse. Radiative cooling is less effective because the stellar debris is still highly optically thick in such an early time. Our simulations reveal that a solar-type star with a stellar density profile of $n = 3$ disrupted by a 10^6 solar mass black hole produces ~ 20 clumps of masses in the range of 0.1 to 12 Jupiter masses. The mass fallback rate decays with time, with pronounced spikes from early to late time. The spikes provide evidence for the clumps of the returning debris, while the clumps on the unbound debris can be potentially freely-floating planets and brown dwarfs. This ionization and dissociation induced fragmentation on a tidally disrupted star are a promising candidate mechanism to form low-mass stars to planets around an SMBH.

Keywords: accretion, accretion disks – black hole physics – hydrodynamics – radiative transfer – stars: low-mass – planets and satellites: gaseous planets

1. INTRODUCTION

Supermassive black holes (SMBHs) reside ubiquitously at the center of galaxies, based on observations of stellar proper motion, stellar velocity dispersion or accretion luminosity (Kormendy & Ho 2013). Tidal disruption events (TDEs) are thought to be a key signature of dormant SMBHs at the centers of the inactive galaxies or intermediate-mass black holes (IMBHs) in star clusters. As a star approaches to a SMBH, it is torn apart by the tidal force of the black hole, which dominates the self-gravity of the star at the tidal disruption radius:

$$r_t = \left(\frac{M_{\text{bh}}}{m_*}\right)^{1/3} r_* \approx 24 \left(\frac{M_{\text{bh}}}{10^6 M_\odot}\right)^{-2/3} \left(\frac{m_*}{M_\odot}\right)^{-1/3} \left(\frac{r_*}{R_\odot}\right) r_s. \quad (1)$$

Here we denote the black hole mass with M_{bh} , stellar mass with m_* and radius with r_* , and the Schwarzschild radius with $r_{\text{S}} = 2GM_{\text{bh}}/c^2$, where G and c are Newton’s gravitational constant and the speed of light, respectively. Most TDEs take place when a star at large separation (~ 1 pc) is perturbed onto a parabolic orbit approaching close enough to the SMBH to be ripped apart by its tidal force. The subsequent accretion of stellar debris falling back to the SMBH produces a characteristic flare with a luminosity that could exceed the Eddington luminosity for a time scale of weeks to months (Rees 1988; Phinney 1989; Evans & Kochanek 1989).

TDE flares have been discovered at optical, ultraviolet, and soft X-ray (see Komossa 2015 for a review; Holoien et al. 2016; Auchettl et al. 2017) wavelengths with infrared event rates of $10^{-5} - 10^{-4}$ per year per Milky-way mass galaxy (Donley et al. 2002; Stone & Metzger 2016), while jetted TDEs have been detected through non-thermal emissions in radio (Zauderer et al. 2011; Alexander et al. 2016; van Velzen et al. 2016) or hard X-ray (Burrows et al. 2011; Brown et al. 2015), with a lower event rate (Farrar & Piran 2014; Dai & Fang 2017). Some spectroscopic researches confirmed H I and He II (Arcavi et al. 2014) as well as metal lines (Leloudas et al. 2019) in TDEs. Weakly relativistic blue-shifted broad absorption lines were attributed to a high-velocity outflow produced in TDE AT2018zr (Hung et al. 2019).

It is still debated how the expected fallback rate as a function of time, $\propto t^{-5/3}$, translates into the observed light curves. While most of the soft X-ray TDEs appear to follow the $t^{-5/3}$ scaling, the optical to ultraviolet TDEs exhibit the different decay (e.g., Gezari et al. 2012). Lodato et al. (2009) numerically showed that the fallback rate depends on the internal structure of the tidally disrupted star, leading to early-time deviations from the standard behavior. The centrally condensed core survived by the partial disruption of the star can make the light curve steeper (Guillochon & Ramirez-Ruiz 2013). The accretion of clumps formed by self-gravitational fragmentation of the debris stream causes the significant variations of the light curve around the $t^{-5/3}$ average at very late time (Coughlin & Nixon 2015), although they did not explain the underlying trigger for the self-gravitating instability. These clumps could be the origin of G2 cloud observed around Sgr A* (Guillochon et al. 2014), which made the clumpy structure on the debris by a fluid instabilities caused by the interaction between the debris stream and an ambient medium.

In this paper, we explore the possibility of rapid fragmentation of a tidally disrupted star around a SMBH through radiation hydrodynamic (RHD) simulations. In section 2, we describe our numerical approach, focusing on the radiation transfer we make use of. In section 3, we study what causes rapid fragmentation of stellar debris, and predict the resulting fallback rate. Finally, section 4 concludes with a discussion of our results and their implication.

2. COMPUTATIONAL METHOD

We start by describing our numerical methods, with a focus on how we handle the radiation transfer in the numerical code, and summarize the setup of our physical and numerical models. The simulations presented below were performed using a three-dimensional (3D), Smoothed Particle Hydrodynamics (SPH) code with radiative transfer. The code is based on the original version of Benz (1990); Benz et al. (1990), but substantially modified as described in Bate et al. (1995) and parallelized using both OpenMP and MPI. Subsequently, the radiation hydrodynamics was incorporated into the code by Whitehouse & Bate (2004) and Whitehouse et al. (2005), and it has been used extensively to study star formation (e.g Whitehouse & Bate 2006; Bate 2012).

2.1. *Equations of radiation hydrodynamics in SPH*

In a frame comoving with a radiating fluid, assuming the local thermodynamics equilibrium (LTE), the equations of self-gravitating, non-viscous RHD to order unity in v/c are given by (Turner & Stone 2001; Whitehouse & Bate 2004; Whitehouse et al. 2005),

$$\frac{D\rho}{Dt} = -\rho\nabla \cdot \mathbf{v}, \quad (2)$$

$$\rho \frac{D\mathbf{v}}{dt} = -\nabla p + \frac{\chi_F \rho}{c} \mathbf{F} - \rho \nabla \phi, \quad (3)$$

$$\rho \frac{D}{Dt} \left(\frac{e}{\rho} \right) = -p \nabla \cdot \mathbf{v} - 4\pi \kappa_p \rho B + c \kappa_E \rho E, \quad (4)$$

$$\rho \frac{D}{Dt} \left(\frac{E}{\rho} \right) = -\nabla \cdot \mathbf{F} - \nabla \mathbf{v} : \mathbf{P} + 4\pi \kappa_p \rho B - c \kappa_E \rho E, \quad (5)$$

$$\frac{\rho}{c^2} \frac{D}{Dt} \left(\frac{\mathbf{F}}{\rho} \right) = -\nabla \cdot \mathbf{P} - \frac{\chi_F \rho}{c} \mathbf{F}, \quad (6)$$

$$\nabla^2 \phi = 4\pi G \rho, \quad (7)$$

where $D/Dt \equiv \partial/\partial t + \mathbf{v} \cdot \nabla$ is the convective derivative, ρ is the density, \mathbf{v} is the velocity, e is the specific energy of the gas, p is the scalar isotropic pressure of the gas, ϕ is the gravitational potential, B is the frequency-integrated Planck function, E is the frequency-integrated radiation energy, \mathbf{F} is the momentum flux density, \mathbf{P} is the radiation pressure tensor. The colon product: $\nabla \mathbf{v} : \mathbf{P}$ indicates contraction over two indices as follows: $(\partial v_j / \partial x_i) P_{ij}$.

Note that equations (3)-(5) have been integrated over frequency. This leads to the flux mean opacity χ_F , the Planck mean opacity κ_P , and the energy mean opacity κ_E . The opacities are assumed to be independent of frequency so that $\kappa_P = \kappa_E$, and they are newly defined as κ without the subscripts. The total opacity, χ_F , should be the sum of the components of κ and scattering. In our simulations, we ignore the scattering so that $\chi_F = \kappa$.

 2.1.1. *Flux-limited diffusion*

The flux-limited diffusion method provides the following relation (Levermore & Pomraning 1981),

$$\mathbf{F} = -\mathcal{D} \nabla E, \quad (8)$$

with a diffusion constant $\mathcal{D} = c\lambda(E)/(\chi\rho)$, where $\lambda(E)$ is the flux limiter, as an alternative of equation (6). It assumes a radiation pressure stress tensor,

$$\mathbf{P} = \mathbf{f} E, \quad (9)$$

where \mathbf{f} is the Eddington tensor:

$$\mathbf{f} = \frac{1}{2}(1 - f(E))\mathbf{I} + \frac{1}{2}(3f(E) - 1)\hat{\mathbf{n}}\hat{\mathbf{n}}, \quad (10)$$

with isotropic unit tensor \mathbf{I} and unit vector $\hat{\mathbf{n}} = \nabla E/|\nabla E|$ in the direction of radiation energy gradient. Here, $f(E)$ is the Eddington factor:

$$f(E) = \lambda(E) + \lambda^2(E)\mathcal{R}(E)^2, \quad (11)$$

where $\mathcal{R}(E) = |\nabla E|/(\chi\rho E)$ is the dimensionless quantity and we choose the flux limiter of [Levermore & Pomraning \(1981\)](#):

$$\lambda(E) = \frac{2 + \mathcal{R}(E)}{6 + 3\mathcal{R}(E) + \mathcal{R}^2(E)}. \quad (12)$$

We solve the RHD equations by using equations (8)-(12) without solving equation (6) directly.

2.1.2. Equation of state and opacities

In order to close the equations (2)-(12), we need to add the equation of state for the gas:

$$p = \mathcal{E}(T)\rho \quad (13)$$

where $\mathcal{E}(T)$ is a specific internal energy. Note that $\mathcal{E}(T)$ equals to $(R_g/\mu)T$ for an ideal gas, where R_g is the gas constant and μ is the molecular weight. For pure hydrodynamic simulations an adiabatic equation of state

$$p = K\rho^\gamma \quad (14)$$

is used in addition to the ideal equation of state, where γ is the specific heat ratio ($\gamma = 5/3$ is applied for a monoatomic gas) and K is a proportionality constant. On the other hand, when the ionization and dissociation of the molecular hydrogen and hydrogen is included, [Black & Bodenheimer \(1975\)](#) derived:

$$\begin{aligned} \mathcal{E}(T) = & X(1 - y)E(H_2)T + [1.5X(1 + x)y + 0.375Y(1 + z_1 + z_1z_2)]R_gT \\ & + X(1.304 \times 10^{13}x + 2.143 \times 10^{12})y + Y(5.888 \times 10^{12}(1 - z_2) + 1.892 \times 10^{13}z_2)z_1, \end{aligned} \quad (15)$$

where X and Y are the mass fractions of hydrogen and helium, respectively, y is the dissociation fraction of hydrogen, x the ionization fraction of hydrogen, and z_1 and z_2 are the degrees of single and double ionization of helium, respectively. $E(H_2)$ gives the contribution to the specific heat capacity from molecular hydrogen and the ionization fractions are calculated using the standard Saha equation ([Black & Bodenheimer 1975](#); [Boley et al. 2007](#)). The mean molecular weight also changes with the degree of the ionization and dissociation, and was derived by [Black & Bodenheimer \(1975\)](#),

$$\mu = \frac{4}{2X(1 + y + 2xy) + Y(1 + z_1 + z_2)}. \quad (16)$$

In our simulations, the solar elemental composition ($X = 0.70$ and $Y = 0.28$) are applied and the mean molecular weight of the gas is initially $\mu = 2.38$ for this composition ([Bate 2012](#)).

We adopt the gas opacity tables from [Alexander \(1975\)](#) and the dust opacity from [Pollack, McKay & Christofferson \(1985\)](#), and from [Ferguson et al. \(2005\)](#) at the higher temperatures when the dust is sublimated. Above 10^4 K, the opacity is dominated by the Kramers law and electron scattering:

$$\kappa = \kappa_K + \kappa_{es} = 1.2512 \times 10^{22} \rho T^{-7/2} + 0.4 \text{ cm}^2 \text{ g}^{-1}. \quad (17)$$

For temperatures above a few million K, the opacity, specific heat capacity, and mean molecular mass approach constant values.

Table 1. Simulated models of TDEs. The first column shows the model label. The second column is the polytropic index, n , of gas sphere at the initial setting. The third column indicates whether radiative transfer was used. The fourth and fifth columns provide the number of clumps and the clump’s mass, respectively. The last column describes the type of corresponding simulation.

Model	Polytropic index n	Radiative transfer	Fragmentation at $t = 100$	Clumpy number N_{cl}	Remark
S1	1.5	–	no	0	Pure Hydro.
S2	1.5	on	no	0	RHD
S3	3	–	no	0	Pure Hydro.
S4	3	on	yes	16	RHD
S5	3	off	yes	19	RHD

2.2. Modeling stellar tidal disruption by SPH with radiative transfer

We follow two-stages in studying the process of tidal disruption of a virialized star by a SMBH. In the first stage, we model a star by the polytrope, which is a solution to the Lane-Emden equation with a polytropic index $n = 1.5$ and $n = 3$ as an initial condition. We then run five types of simulations of a solar-type star with mass and radius $(m_*, r_*) = (1 M_\odot, 1 R_\odot)$, and a solar metallicity ($1 Z_\odot$) for the RHD cases. We finish the simulations at $t = 50$ when they are well-virialized, where the unit of time is given by $\Omega_*^{-1} = \sqrt{r_*^3/Gm_*} \simeq 1.6 \times 10^3$ s. Models S1 and S3 show the purely hydrodynamic simulations with $n = 1.5$ and $n = 3$, respectively, whereas Model S2 represents the RHD simulation of the polytrope of $n = 1.5$. Models S4 and S5 do the RHD simulations of an $n = 3$ polytrope with and without radiative transfer. The details of each model are shown in Table 1. For all models, the magnitude ratio of thermal to gravitational energies ranges between $0.497 \leq |E_{\text{th}}/E_{\text{grav}}| \leq 0.499$ at $t = 0$ and takes a value of $|E_{\text{th}}/E_{\text{grav}}| = 0.497$ at $t = 50$. It means that stars that we make use of in the second-stage are well-virialized.

In the second stage, the SMBH is added at the origin and the star is initially located at the distance of three times its tidal disruption radius from the black hole. The total number of SPH particles used in each simulation is $\sim 10^6$. In all second-stage simulations, we used $M_{\text{bh}} = 10^6 M_\odot$, $m_* = 1 M_\odot$, $r_* = 1 R_\odot$, and termination time of each simulation is $t = 100$. Figure 1 depicts the radial density distribution of the stellar debris for the five models and the radial temperature distribution of Models 3 and 4. Panel (a) represents that of Models S1 and S2 at $t = 0$, whereas panel (b) does that of Models S1 and S2 at $t = 100$. Panel (c) represents that of Models S3 and S4 at $t = 0$, whereas panel (d) does that of Models S3 and S4 at $t = 100$. Panel (e) represents the corresponding temperature distribution to panel (d). For comparison, panel (d) represents the overlapped density distribution between those of Models S4 and S5. Panel (a) shows that Model S1 initially have the same density profile as Model S2, while panel (c) shows that Models S3 initially have the same density profile as Model S4. Note that Model S5 has also the same density profile at $t = 0$ as those of Models S3 and S4.

3. FRAGMENTATION OF THE STELLAR DEBRIS

Panel (b) of Figure 1 indicates that no fragmentation is apparent at $t = 100$ for the $n = 1.5$ cases, although some structure is seen around the highest density region of Model S2. It is apparent

from panel (d) that the stellar debris remarkably fragments in Model S4, whereas it shows no clear fragmentation in Model S3. This demonstrates that a remarkable fragmentation occurs at $t = 10^5 \text{ s} \sim 1 \text{ day}$, soon after tidal disruption of the star modeled by a $n = 3$ polytrope. In panel (d), the dashed line denotes $\rho_{\text{crit}} = 3 \times 10^{-3} \text{ g cm}^{-3}$, which we set as a fiducial minimum value for defining a clump. The fourth to sixth columns of Table 1 shows the flag of whether the debris fragments at $t = 100$, the number of clumps (N_{cl}), and the type of corresponding simulation, respectively. Figure 2 shows the density map of the stellar debris of Models S3 and S4 at $t = 100$ in the x-y plane over a dynamic range of twelve orders of magnitude. Each axis is normalized by the tidal disruption radius. The black hole is located at the origin. The figure demonstrates that there are ~ 20 clumps on the debris in Model S4, whereas it is obvious that there is no fragmentation in Model 3. These results are consistent with panel (d).

We find from panel (e) that in Model S3 the gas temperature in the bulk of the debris filament (i.e. not in the clumps) is substantially higher than in the Model S4 case, and that is why the debris filament does not fragment (because the temperature is typically higher at a given density) in Model S3. It suggests that some mechanism should efficiently work to make the stellar debris cools down. One of promising mechanisms is radiative cooling. If the debris is fully ionized, its optical depth for Thomson scattering is estimated to be,

$$\tau_p = n_p \sigma_T r \approx 2 \times 10^9 \left(\frac{\rho}{10^{-3} \text{ g cm}^{-3}} \right) \left(\frac{r}{r_t} \right), \quad (18)$$

where $n_p \approx \rho/m_p$ is the number density of the free electrons, m_p is the proton's mass, and σ_T is the Thomson scattering cross section. This implies that radiative cooling is not efficient because the opacity of the gas is so high that the photon diffusion time is very long. Panel (f) demonstrates that radiative cooling does not work as a debris cooling mechanism almost at all because the stellar debris clearly fragments in Model S5 as well as Model S4.

Figure 3 includes six panels in Model 4: panel (a) provides the gas temperature distribution over the density. The temperature ranges from $\sim 3 \times 10^3 \text{ K}$ to $4 \times 10^4 \text{ K}$ over $1.0 \times 10^{-4} \text{ g cm}^{-3} \leq \rho \lesssim 1.0$. The gas temperature tends to increase with the density. Panel (b) depicts the temperature dependence of the ratio of the pressure computed by equation 13 to the pressure of the corresponding ideal gas. The panel indicates that the gas pressure can be significantly weaker than the ideal gas case at some temperature range, where the gravitational collapse can occur. We find from panel (c) that the mean molecular weight changes in two stages: first, it changes due to the dissociation of H_2 from 2.38 to $1.3 \sim 1.5$ in the range of $3 \sim 5 \times 10^3 \text{ K}$. Next, due to the hydrogen ionization, the mean molecular weight starts at $\sim 3 \times 10^4 \text{ K}$ decreasing to 0.61, where the gas is fully ionized. In panel (d), the smoothing length is 0.25 times smaller than R_J for more than $10^{-4} \text{ g cm}^{-3}$. We denote from the panel that the clumps on the debris seen in Figure 2 are numerically sufficiently resolved.

In panel (e), the Jeans radius is defined by

$$R_J = \sqrt{\frac{3}{8\pi}} \left(\frac{R_g}{G\mu} \right)^{1/2} \left(\frac{T}{\rho} \right)^{1/2}, \quad (19)$$

where we assume that the mean density of a clump corresponds to the density of each SPH particle. With R_J estimated from equation (19), the Jeans mass is given by

$$M_J = \frac{1}{2} \frac{R_J c_s^2}{G} = \frac{1}{2} \left(\frac{R_g}{\mu G} \right) T R_J. \quad (20)$$

From the panel, the Jeans mass is distributed over $0.1 < M_J/M_{\text{Jup}} < 12$ and the Jeans radius is distributed over $2 < R_J/R_{\text{Jup}} < 20$. According to Burrows et al. (2007), the observed mass-radius relation of giant planets occupies the narrow range of $0.76 \lesssim r_{\text{cl}}/R_{\text{Jup}} \lesssim 1.4$ for $0.35 \lesssim m_{\text{cl}}/M_{\text{Jup}} \lesssim 1.35$, where r_{cl} and m_{cl} are the radius and mass of the formed clump, respectively. For brown dwarfs at age of \sim Gyr, the observed mass-radius relation shows $0.9 < r_{\text{cl}}/R_{\text{Jup}} < 1.1$ for $2 \leq m_{\text{cl}}/M_{\text{Jup}} \leq 20$ (Burrows et al. 2011). In our simulations, the returning clumps having the orbital period less than ~ 100 yr are too hot to cool down to be the observed giant planets, while the unbound clumps can be potentially freely-floating planets and brown dwarfs if they would keep surviving.

The ratio of stellar to clump's tidal disruption radii is given by

$$\frac{r_{\text{t,cl}}}{r_{\text{t}}} = \left(\frac{m_*}{m_{\text{cl}}}\right)^{1/3} \frac{r_{\text{cl}}}{r_*} \sim 1.02 \left(\frac{m_*}{M_{\odot}}\right)^{1/3} \left(\frac{r_*}{R_{\odot}}\right)^{-1} \left(\frac{m_{\text{cl}}}{M_{\text{Jup}}}\right)^{-1/3} \left(\frac{r_{\text{cl}}}{R_{\text{Jup}}}\right), \quad (21)$$

where r_{cl} and m_{cl} are the clumpy radius and mass, and the tidal disruption radius of a clump is given by

$$r_{\text{t,cl}} = \left(\frac{M_{\text{bh}}}{m_{\text{cl}}}\right)^{1/3} r_{\text{cl}}. \quad (22)$$

Panel (f) shows that the tidal radius of the returning clumps is larger than the tidal radius of the original star. This suggests that all the returning clumps would be tidally disrupted. If the returning clump is disrupted, then the subsequent flare would be triggered after the orbital period of the returning debris on the most tightly bound orbit:

$$t_{\text{mtb,cl}} = \frac{\pi}{\sqrt{2}} \left(\frac{M_{\text{bh}}}{m_{\text{cl}}}\right)^{1/2} \frac{1}{\Omega_{\text{cl}}} \approx 1.2 \times 10^8 \text{ s} \left(\frac{M_{\text{bh}}}{10^6 M_{\odot}}\right)^{1/2} \left(\frac{m_{\text{cl}}}{M_{\text{Jup}}}\right)^{-1} \left(\frac{r_{\text{cl}}}{R_{\text{Jup}}}\right)^{3/2}, \quad (23)$$

where $\Omega_{\text{cl}} = \sqrt{Gm_{\text{cl}}/r_{\text{cl}}^3}$ is the dynamical angular frequency of the clump. The peak fallback rate is then estimated to be

$$\dot{M}_{\text{cl,max}} = \frac{1}{3} \frac{m_{\text{cl}}}{t_{\text{mtb,cl}}} \sim 8.5 \times 10^{-5} M_{\odot} \text{ yr}^{-1} \left(\frac{M_{\text{bh}}}{10^6 M_{\odot}}\right)^{-1/2} \left(\frac{m_{\text{cl}}}{M_{\text{Jup}}}\right)^2 \left(\frac{r_{\text{cl}}}{R_{\text{Jup}}}\right)^{-3/2}. \quad (24)$$

By taking account of the range of simulated mass and radius of the formed clump, which is obtained from panel (b), equation (24) implies that the tidal disruption of the fallback clumps would be smaller than the Eddington accretion rate $\dot{M}_{\text{Edd}} = L_{\text{Edd}}/c^2 \sim 2.2 \times 10^{-3} M_{\odot} \text{ yr}^{-1} (M_{\text{bh}}/10^6 M_{\odot})$, where $L_{\text{Edd}} = 4\pi GM_{\text{bh}}m_p c/\sigma_{\text{T}}$ is the Eddington luminosity.

Figure 4 is the simulated mass fallback rate of the stellar debris for each model. The mass fallback rate is defined by $\dot{M}_{\text{fb}} = (dM/d\epsilon)(d\epsilon/dt)$, where ϵ is the specific energy of the stellar debris, $d\epsilon/dt \propto t^{-5/3}$ because of Kepler's third law, and $dM/d\epsilon$ is the simulated differential mass distribution. The solid black and red lines show the mass fallback rates of Models S4 and S5, while the dotted green and dashed blue line represents that of Model S3 and the standard $t^{-5/3}$ decay rate. The horizontal dashed orange line shows the Eddington accretion rate. The mass fallback rates of Models S4 and S5 decays with several pronounced spikes from the early to late time. The spikes in the light curve can be used as evidence for the clump formation in TDEs.

4. DISCUSSIONS AND CONCLUSIONS

We have performed the RHD simulations of tidal disruption of a star on a parabolic orbit by a SMBH by using a 3D SPH code with radiative transfer. Our conclusions are as follows:

1. Tidally disrupted stars fragment and form ~ 20 clumps soon after tidal disruption (~ 1 day for an SMBH of $10^6 M_\odot$). This formation is triggered by the endothermic processes through ionization and dissociation of helium and hydrogen, decreasing the gas pressure compared with the adiabatic gas case, leading to local gravitational collapse. Radiative cooling is ineffective almost at all in causing fragmentation because the stellar debris is highly optically thick.
2. The fragmentation does not occur in tidal disruption of a star modeled as a $n = 1.5$ polytrope. This is because the highest density is an order of magnitude lower than that of $n = 3$ case.
3. The mass fallback rate decays with time but shows several pronounced spikes due to the formation of clumps. The detection of such spikes can serve as a smoking-gun for clump formation in stellar debris.
4. The clumps on unbound debris can be potentially freely-floating planets and brown dwarfs.

We have also tested the dependence of the debris fragmentation for the $n = 3$ case on the penetration factor β , and found that it occurs only for $\beta \gtrsim 2.2$. This condition resembles the condition for avoiding the partial tidal disruption, where the core of the star survives (Mainetti et al. 2017). We find that if the fraction of SPH particles making of the central, biggest clump is less than one-third of the total particle number, the debris can fragment. The degree of central concentration determines whether the stellar debris fragments or not. This is possibly due to the suppression of the self-gravitating instability by the central clump. The suppression condition is given by the balance between the self-gravity of the smaller clump and the gravity acting on it from the central clump as $Gm_{\text{cl}}^2/r_{\text{cl}}^2 \lesssim Gm_c m_{\text{cl}}/r^2(H/r)$, where m_c , H , and r is the mass of the central clump, the debris scale height, and the distance between the the central and the other clumps. Because this results in $r/r_{\text{cl}} \lesssim (m_c/m_{\text{cl}})^{1/2}(H/r)^{1/2} \sim \mathcal{O}(1)$, we find the suppression by the central clump cannot work. If the originally approaching star is more massive than $10R_\odot$, then each clump's mass should correspond to a star. This is a promising mechanism for making low-mass stars around a SMBH or an IMBH.

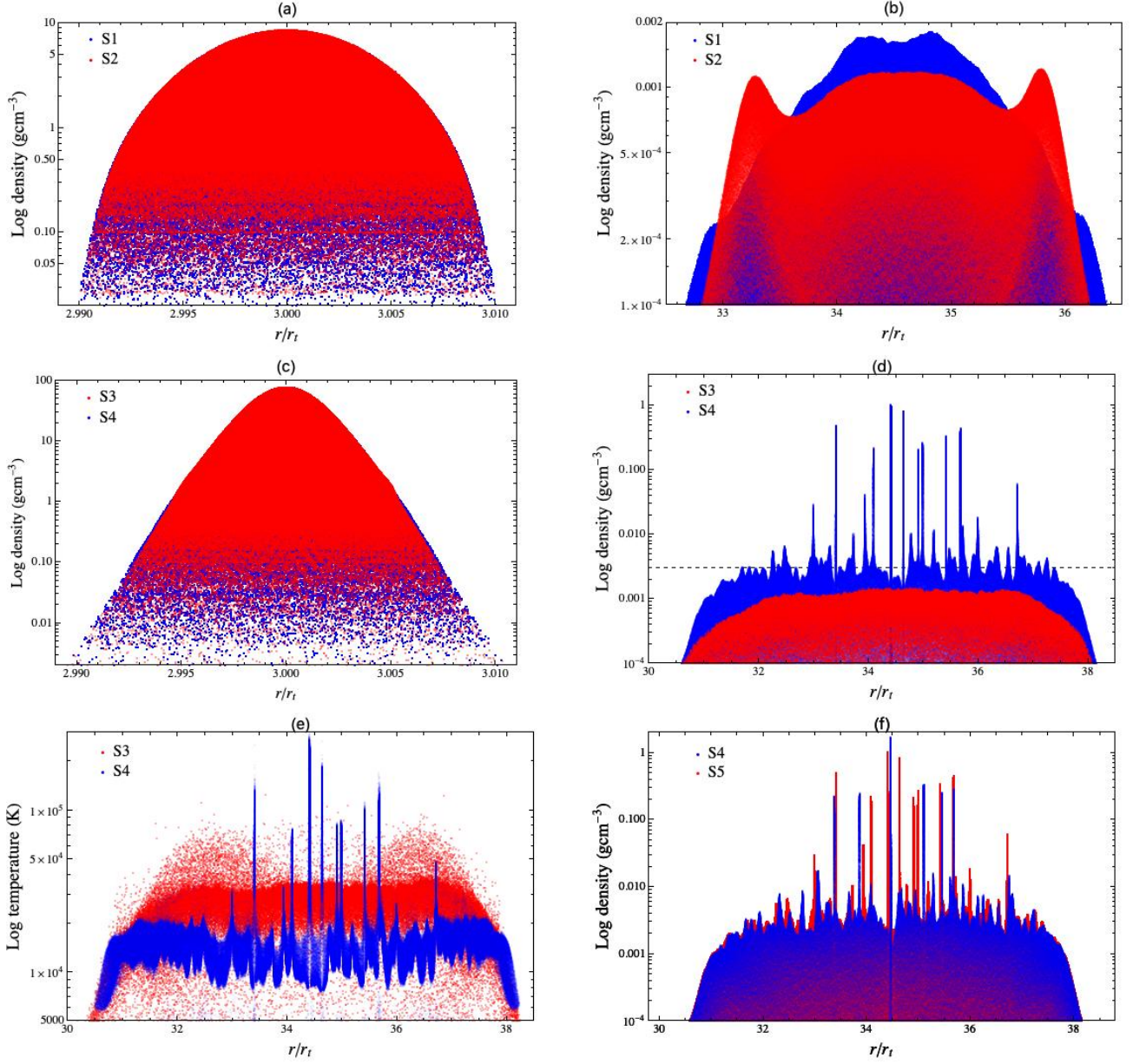


Figure 1. Radial density distributions of the star at $t = 0$ and of the stellar debris at $t = 100$. Panel (a) shows the overlapped density distribution between Models S1 and S2 at $t=0$, while panel (b) shows the same distribution as panel (a) but for at $t=100$. Panel (c) shows the overlapped density distribution between Models S3 and S4 at $t=0$, while panel (d) shows the same distribution as panel (c) but for at $t=100$. In panel (d), the dashed line represents $\rho_{\text{crit}} = 3 \times 10^{-3} \text{ g cm}^{-3}$, which is set as a fiducial value of the gas density. We then recognize what has the density beyond it as a clump. Panel (e) depicts the corresponding temperature distribution to panel (d). Panel (f) represents the overlapped density distribution between Models S4 and S5 at $t = 100$.

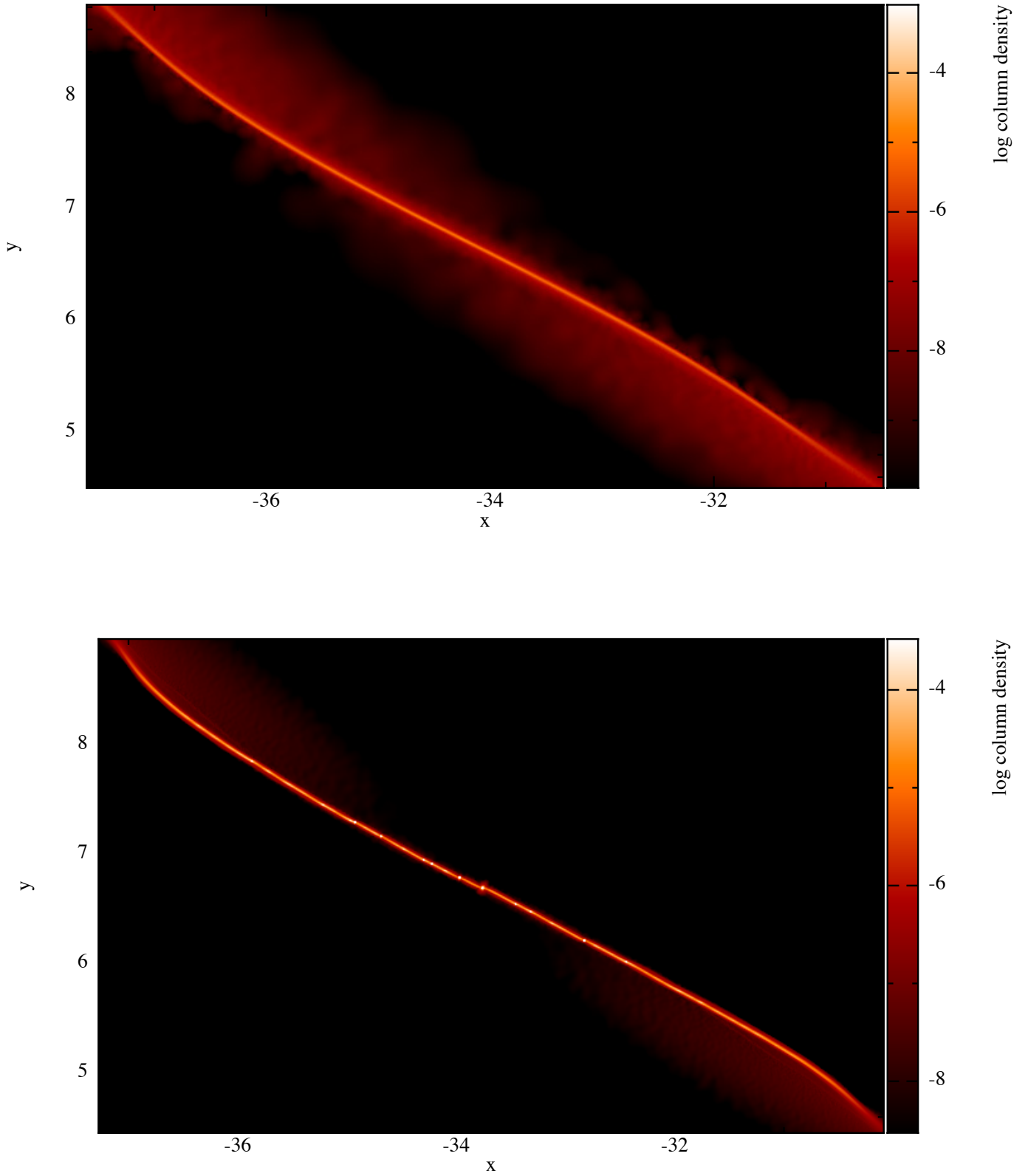


Figure 2. Density map of the stellar debris of Models S3 and S4 at $t = 100$ in the x - y plane over the twelve orders of magnitude logarithmic scale in computational unit. Each axis is normalized by the tidal disruption radius. The black hole is located at the origin.

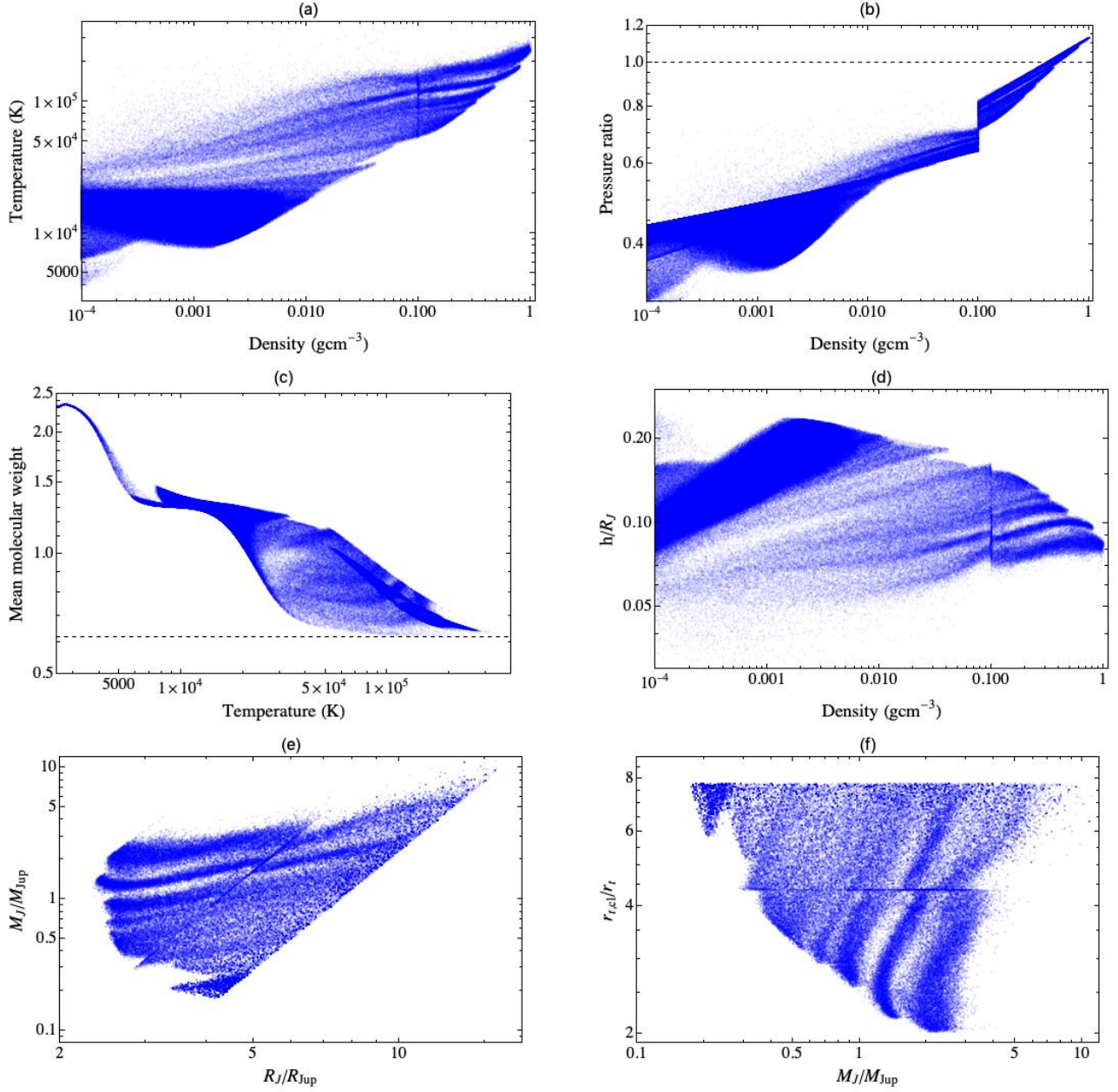


Figure 3. SPH particle distributions in some phase-spaces of Model 4 at $t=100$. In all the panels, each axis is shown on a logarithmic scale. (a) Gas temperature-density distribution (b) Density dependence of the ratio of the pressure computed by equations 13 and 15 to the pressure of the corresponding ideal gas. (c) Mean molecular weight-temperature distribution. The dashed line denotes $\mu_0 = 0.62$, which corresponds to the mean molecular weight for the fully ionized gas. (d) Dependence of the smoothing length normalized by R_J on the gas density. (e) Jeans mass-radius distribution for $\rho \geq \rho_{\text{crit}}$, where $\rho_{\text{crit}} = 3 \times 10^{-3} \text{gcm}^{-3}$. The Jeans radius and mass are normalized by Jupiter's radius R_{Jup} and mass M_{Jup} , respectively. (f) Dependence of the ratio of stellar to clump's tidal disruption radii (see equation 21) on Jeans mass.

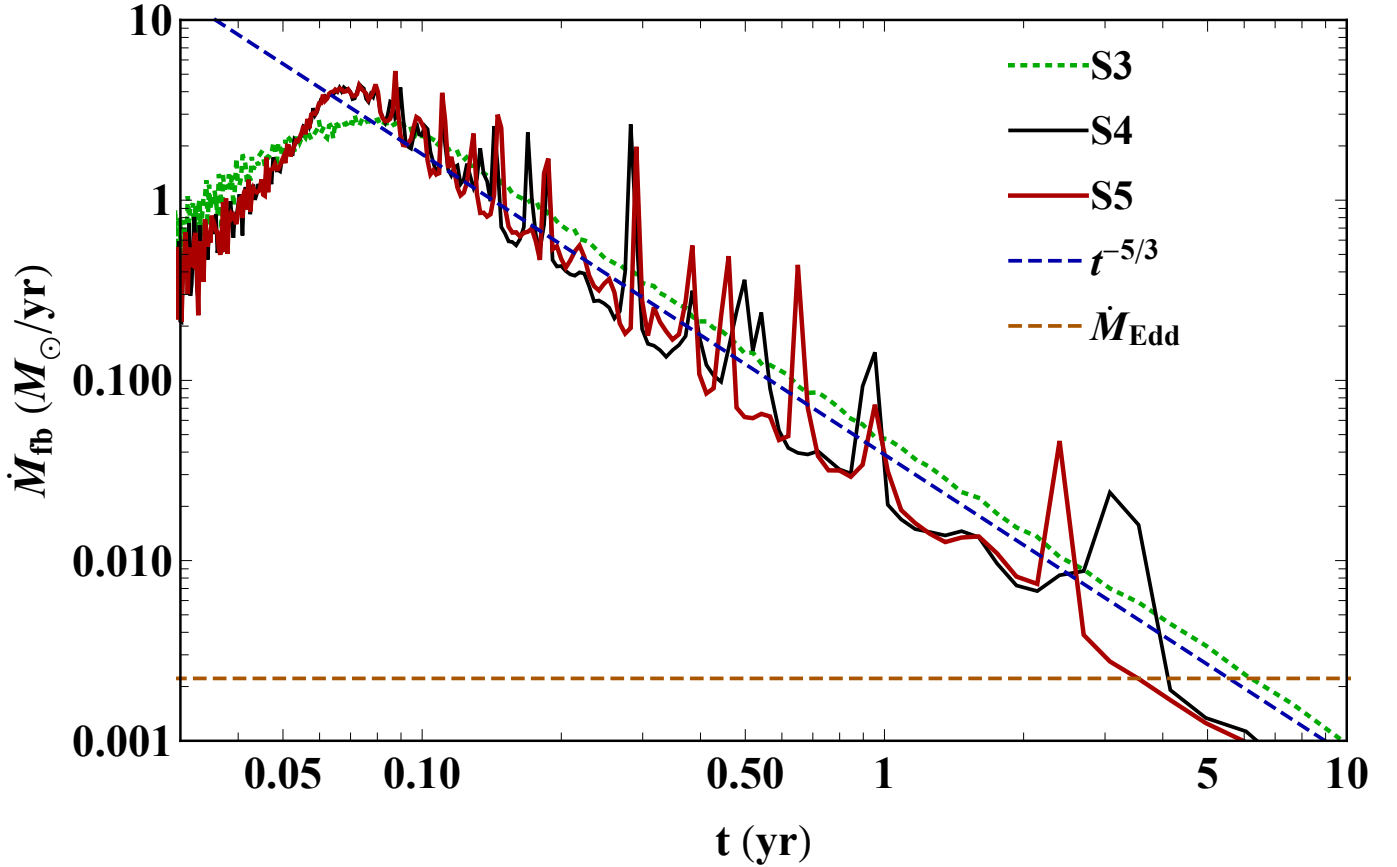


Figure 4. Simulated mass fallback rates of the stellar debris. The solid black and red lines show that of Models S4 and S5, while the dotted green and dashed blue line represents that of Model S3 and the standard $t^{-5/3}$ decay rate. The horizontal dashed orange line shows the corresponding Eddington accretion rate.

ACKNOWLEDGMENTS

This research has been supported by Basic Science Research Program through the National Research Foundation of Korea (NRF) funded by the Ministry of Education (NRF-2016R1A5A1013277 and 2017R1D1A1B03028580 to KH), by the European Research Council under the European Communitys Seventh Framework Programme (FP7/2007- 2013 grant agreement no. 339248 MRB), and by the Black Hole Initiative at Harvard university which is funded by JTF and GBMF (AL). The numerical simulations were performed and also supported by the National Supercomputing Center with supercomputing resources including technical support (KSC-2019-CRE-0082 to KH).

REFERENCES

- Alexander D. R., 1975, *ApJS*, 29, 363
 Alexander, K. D., Berger, E., Guillochon, J., Zauderer, B. A., & Williams, P. K. G. 2016, *ApJL*, 819, L25
 Arcavi I. et al., 2014, *ApJ*, 793, 38
 Auchettl, K., Guillochon, J., & Ramirez-Ruiz, E. 2017, *ApJ*, 838, 149
 Bate, M. R., Bonnel, I. A., Price, N.M., 1995, *MNRAS*, 277, 362
 Bate, M. R. 2012, *MNRAS*, 419, 3115
 Benz W., 1990, in the *Numerical Modeling of Nonlinear Stellar Pulsations: Problems and Prospects*, ed. Buchler, R.J. (Dordrecht: Kluwer Academic Publishers), 269

- Benz, W., Bowers, R.L., Cameron, A.G.W.,
Press, W.H., 1990, *ApJ*, 348, 647
- Black D. C., Bodenheimer P., 1975, *ApJ*, 199, 619
- Boley, A. C., Hartquist, T. W., Durisen, R. H., et al. 2007, *ApJL*, 656, L89
- Brown, G. C., Levan, A. J., Stanway, E. R., et al. 2015, *MNRAS*, 452, 4297
- Burrows, A., Hubeny, I., Budaj, J., et al. 2007, *ApJ*, 661, 502
- Burrows, A., Heng, K., & Nampaisarn, T. 2011, *ApJ*, 736, 47
- Burrows D. N. et al., 2011, *Nature* 476, 421
- Coughlin, E. R., & Nixon, C. 2015, *ApJL*, 808, L11
- Dai, L., & Fang, K. 2017, *MNRAS*, 469, 1354
- Donley J. L., Brandt W. N., Eracleous M.,
Boller T., 2002, *AJ*, 124, 1308
- Evans C.R., Kochanek C.S., 1989, *ApJ*, 346, L13
- Farrar, G. R., & Piran, T. 2014, arXiv:1411.0704
- Ferguson et al., 2005, *ApJ*, 623, 585
- Gezari, S., Chornock, R., Rest, A., et al. 2012, *Nature*, 485, 217
- Guillochon, J., & Ramirez-Ruiz, E. 2013, *ApJ*, 767, 25
- Guillochon, J., Loeb, A., MacLeod, M., & Ramirez-Ruiz, E. 2014, *ApJL*, 786, L12
- Holoien, T. W.-S., Kochanek, C. S., Prieto, J. L., et al. 2016, *MNRAS*, 455, 2918
- Hung, T., Cenko, S. B., Roth, N., et al. 2019, arXiv e-prints, arXiv:1903.05637.
- Komossa, S. 2015, *Journal of High Energy Astrophysics*, 7, 148
- Kormendy, J., Ho, L. C., 2013, *ARA&A*, 51, 511
- Leloudas, G., Dai, L., Arcavi, I., et al. 2019, arXiv e-prints, arXiv:1903.03120
- Levermore C. D., Pomraning G. C., 1981, *ApJ*, 248, 321
- Lodato, G., King, A.R., Pringle, J.E. 2009, 392, 332
- Mainetti, D., Lupi, A., Campana, S., et al. 2017, *Astronomy and Astrophysics*, 600, A124
- Phinney, E. S. 1989, in *IAU Symp. 136, The Center of the Galaxy*, ed. M. Morris (Dordrecht: Kluwer Academic Publishers), 543
- Pollack J. B., McKay C. P., Christofferson B. M., 1985, *Icarus*, 64, 471
- Rees, M. J., 1998, *Nature* 333, 523
- Stone, N., Metzger, B. D. 2016, *MNRAS*, 455, 859
- Turner N. J., Stone J. M., 2001, *ApJS*, 135, 95
- van Velzen, S., Anderson, G. E., Stone, N. C., et al. 2016, *Science*, 351, 62
- Whitehouse S. C., Bate M. R., 2004, *MNRAS*, 353, 1078
- Whitehouse S. C., Bate M. R., Monaghan J. J., 2005, *MNRAS*, 364, 1367
- Whitehouse S. C., Bate M. R., 2006, *MNRAS*, 367, 32
- Zauderer B. A., et al., 2011, *Nature* 476, 425